

# Gravitational Waves from the Black Hole Seeds and the Assembly of the First Quasars

Yiting Li<sup>1</sup>★, Yuexing Li<sup>2,3,4</sup>, Qirong Zhu<sup>5</sup>, Moupiya Maji<sup>6</sup>, B.S. Sathyaprakash<sup>2,3,7</sup>,  
Raffaella Schneider<sup>4,8</sup>, Hidenobu Yajima<sup>9</sup>, and Lars Hernquist<sup>10</sup>

<sup>1</sup> Department of Physics, University of California, Santa Barbara, CA 94720, USA

<sup>2</sup> Department of Astronomy & Astrophysics, The Pennsylvania State University, University Park, PA 16802, USA

<sup>3</sup> Institute for Cosmology and Gravity, The Pennsylvania State University, University Park, PA 16802, USA

<sup>4</sup> Dipartimento di Fisica, Sapienza, Università di Roma, Piazzale Aldo Moro 5, 00185, Roma, Italy

<sup>5</sup> Department of Physics, Carnegie Mellon University, 5000 Forbes Avenue, Pittsburgh, PA 15213, USA

<sup>6</sup> Observatoire de Genève, Chemin des Maillettes, 51, 1290 Versoix, Switzerland

<sup>7</sup> Department of Physics, The Pennsylvania State University, University Park, PA 16802, USA

<sup>8</sup> INFN, Sezione di Roma I, P.le Aldo Moro 2, 00185 Roma, Italy

<sup>9</sup> Center for Computational Sciences University of Tsukuba, Tsukuba, Ibaraki 305-8577, Japan

<sup>10</sup> Harvard-Smithsonian Center for Astrophysics, Harvard University, 60 Garden Street, Cambridge, MA 02138, USA

Accepted XXX. Received YYY; in original form ZZZ

## ABSTRACT

The next-generation ground- and space-based Gravitational Wave (GW) observatories will offer powerful multi-bandwidth measurements to explore the origin of supermassive black holes (SMBHs) of  $\sim 10^9 M_\odot$  thought to power the most distant quasars observed at redshift  $z \gtrsim 6$ . In a previous study, we performed a suite of cosmological zoom-in simulations of the formation of the first SMBHs with different seeds and growth models. In our new paper, we post-process six of those simulations with BH seeds in the mass range of  $10 - 10^6 M_\odot$  to investigate the GW signals from the assembly of SMBHs. We extract the merger history of BHs from each simulation, and employ a phenomenological waveform model to compute the GW strains and signal-to-noise ratios from the BH binaries, and estimate the event rates for various GW detectors. We consider both ground-based detectors such as advanced Laser Interferometer Gravitational-Wave Observatory (aLIGO), Einstein Telescope (ET), and Cosmic Explorer (CE), and space-based ones such as Laser Interferometer Space Antenna (LISA), Big Bang Observatory (BBO), and Deci-hertz Interferometer Gravitational wave Observatory (DECIGO). In particular, we provide predictions for the newly proposed “3G” network with three detectors, which include ET-D and two detectors of CE. We find that the “3G” network has the highest potential to detect mergers of low-mass BHs ( $\sim 10 - 10^2 M_\odot$ ) formed from Pop III stars at cosmic dawn  $z \sim 23 - 6$ , while LISA will be able to detect the inspiral and merger events of more massive BHs ( $\sim 10^4 - 10^7 M_\odot$ ) up to  $z \sim 16$ . BBO and DECIGO will bridge the gap between “3G” network and LISA by detecting intermediate-mass BH coalescences ( $\sim 10^2 - 10^4 M_\odot$ ) in the same epoch. Our results demonstrate that a synergy between ground- and space-based detectors may be able to detect  $\sim 10\%$  of all the BH mergers in the mass range of  $\sim 10^1 - 10^7 M_\odot$  at redshifts  $z \sim 23 - 6$ , which will provide unmatched insights into the seeds and growth histories of the first SMBHs and quasars in the early Universe.

**Key words:** gravitational waves – cosmology – black hole – quasars – early universe – numerical

## 1 INTRODUCTION

Gravitational waves (GWs), first predicted by Einstein in 1916 in his general theory of relativity, are “ripples” in the curvature

of spacetime generated by massive accelerating objects, and they travel at the speed of light like electromagnetic waves (Buonanno & Sathyaprakash 2014). Potential sources of detectable GW signals include catastrophic events such as coalescing compact binaries, core collapse supernovae, and inflation. One hundred years after Einstein’s prediction, GWs were detected for the first time in 2015

★ E-mail: yitingli@ucsb.edu

by the Advanced Laser Interferometer Gravitational-Wave Observatory (aLIGO) (Abbott et al. 2016a). To date, aLIGO and the Advanced Virgo network, which operate in the audio frequency range of  $10 - 10^4$  Hz, has detected about 50 GW events from mergers of binary black holes (BBHs) and binary neutron stars (BNSs) (see Abbott et al. 2020a for the latest catalogue). These ground-breaking discoveries confirm the existence of BHs in the mass range of  $\sim 6 - 150 M_\odot$  (The LIGO Scientific Collaboration et al. 2020).

The LIGO – Virgo discoveries mark the beginning of a new era in GW astronomy with more detectors upcoming. The third generation ground-based interferometers (referred to as “3G”) such as Einstein Telescope (ET, Punturo et al. 2010; Sathyaprakash et al. 2012) and Cosmic Explorer (CE, Abbott et al. 2017; Reitze et al. 2019), which have high sensitivity in frequencies  $\sim 1$  Hz–10 kHz, will be able to detect the GW signal from coalescing BBHs of  $\sim 10 - 10^3 M_\odot$  and a significant fraction at high redshifts up to  $z \gtrsim 20$  (Vitale & Whittle 2018; Kalogera et al. 2019; Maggiore et al. 2020). In this paper we will consider a 3G network comprising of one ET and two CE (one in the US and one in Australia). On the other hand, space-based interferometers such as the Laser Interferometer Space Antenna (LISA, Amaro-Seoane et al. 2017) has a bandwidth of  $10^{-4} - 10^{-1}$  Hz, which will be able to capture massive BH mergers of  $\sim 10^4 - 10^7 M_\odot$  in the epoch of reionization (Colpi et al. 2019). Moreover, the proposed Big Bang Observer (BBO, Crowder & Cornish 2005), the Chinese interferometers TianQin (Luo et al. 2016) and Taiji (Ruan et al. 2018), and the Japanese future space gravitational wave Antenna the Deci-hertz Interferometer Gravitational wave Observatory (DECIGO, Kawamura et al. 2020), will cover a wide frequency range complementary to LISA to detect massive BBHs. These ground- and space-based GW detectors promise to unveil the gravitational universe and BHs throughout cosmic time.

In order to estimate the BH merger rates and predict GW signals for the detectors, a number of groups have explored various methods from analytical or semi-analytical calculations (e.g., Haehnelt 1994; Wyithe & Loeb 2003; Sesana et al. 2004; Barausse et al. 2012; Tanaka et al. 2012; Sesana 2013; Ricarte & Natarajan 2018; Valiante et al. 2020), to the recent cosmological hydrodynamical simulations (e.g., Salcido et al. 2016; Kelley et al. 2017; DeGraf & Sijacki 2020; Siwek et al. 2020; Katz et al. 2020; Volonteri et al. 2020). Analytical and semi-analytical models use simplified assumptions and lack dynamical and spatial information, but they have high flexibility and low computational costs, allowing for parameter studies. On the other hand, cosmological hydrodynamical simulations follow the assembly and dynamical evolution of the systems with complex physical processes, but at high computational cost, so they are usually limited by the number of realizations and numerical resolution. Nevertheless, these works demonstrate that combining cosmological simulations with GW calculations is an effective method to study BHs at different cosmic times.

One limitation of the previous studies using large-scale cosmological simulations is that they have focused only on massive BH seeds of  $10^4 - 10^5 M_\odot$  and their subsequent merger histories. However, smaller BHs may be more populous than massive ones in the early Universe, and they may play a critical role in the assembly of quasars, in particular the distant ones. So far, more than 200 bright quasars have been discovered at redshifts  $z \gtrsim 6$ , with the most distant one being at  $z = 7.54$ , merely  $\sim 700$  Myrs after the Big Bang (see a recent review by Inayoshi et al. 2020). These quasars are believed to be powered by rapidly accreting SMBHs of  $\sim 10^8 - 10^{10} M_\odot$  (e.g., Mortlock et al. 2011; Wu et al. 2015; Bañados et al. 2018; Vito et al. 2019; Inayoshi et al. 2020). However, the formation of these SMBHs within such a short timescale after the

Big Bang is an unsolved puzzle. In particular, it is unclear what the BH seeds were, and how they grew so rapidly.

To date, three seed scenarios have been suggested (see reviews by Inayoshi et al. 2020 and Greene et al. 2020): light seeds  $\sim 10^{1-2} M_\odot$  from Pop III stars (e.g., Madau et al. 2014; Lupi et al. 2016; Valiante et al. 2016, 2017; Pezzulli et al. 2016, 2017), intermediate seeds of  $\sim 10^{3-4} M_\odot$  from the collapse of super-massive stars or stellar collisions (e.g., Katz et al. 2015; Yajima & Khochfar 2016; Woods et al. 2017, 2019), and heavy seeds of  $\sim 10^{5-6} M_\odot$  from the collapse of hot and dense gas clumps called direct collapse black holes (DCBHs) (e.g., Glover 2015a,b; Pacucci et al. 2015; Regan et al. 2017; Wise et al. 2019; Luo et al. 2020).

These seeds may accrete gas and merge with others to grow bigger along with the assembly and dynamical evolution of the host galaxies. In a recent study of the seeds of early quasars, Valiante et al. (2020) used a semi-analytical approach to model the build up of quasars with merger tree realizations of dark matter halos. They found that mergers of small BH seeds of  $\sim 10^2 M_\odot$  may be detectable by 3G observatories at redshifts  $6 < z < 15$ , and then by LISA when they grow to  $10^4 M_\odot$ . RS: They argue that this may be the only chance to discover small BH seeds as the electromagnetic emission associated to their mass growth is too faint to be detectable, even with future facilities (Valiante et al. 2018a,b). Mergers involving massive BH seeds ( $\sim 10^5 - 10^6 M_\odot$ ) may be detectable with LISA up to  $z \sim 20$ , and the combination between 3G observatories and LISA offers a unique insight on the dawn of BH binaries (Valiante et al. 2020).

In a recent study, Zhu et al. (2020) investigated the BH seeds of the observed  $z \gtrsim 6$  quasars. They performed a suite of cosmological zoom-in simulations of a favorable host halo, which has a mass of  $\sim 10^{13} M_\odot$  at  $z = 6$  and a history of multiple major mergers. They tested BH seeds of  $10 - 10^6 M_\odot$  and different accretion models, and found that only massive seeds of mass  $\geq 10^3 M_\odot$  could grow to above  $10^8 M_\odot$  by  $z \sim 6$ , and that many of the BH seeds experienced numerous mergers during dynamical evolution. BSS: It is critical that we say how the current study differs from previous studies, especially Valiante+ 2020 that I am familiar with, and why anyone should care about our results.

Here, we post process six of the simulations in Zhu et al. (2020) with BH seeds in the mass range of  $10 - 10^6 M_\odot$ , to explore the GW signals from BH mergers in the assembly of the first quasars. The paper is organized as follows. In Section 2.1, we describe the cosmological zoom-in simulations, including the BH seed models, the BH merger process, and our treatment of the inspiral phase from the simulations. GW calculations are given in Section 2.2, including the “PhenomD” waveform model, the GW characteristic strain amplitude, and the sensitivity of GW detectors considered in this study. We present the results of our study in Section 3, including the GW characteristic strain amplitudes of seed BH mergers of the first quasars in Section 3.1, their signal-to-noise ratios in Section 3.2, the predicted event rates for a network of GW detectors in Section 3.3, and finally the redshift distribution of resolvable events in Section 3.4. We discuss the limitations of our models in Section 4, and summarize our findings in Section 5.

## 2 METHODS

In this study, we combine cosmological simulations of the formation of the first quasars with GW waveform calculations to compute the gravitational wave amplitude from the inspiral and the merger-ringdown phases of BBH mergers in these simulations. We describe

the hydrodynamical simulations and calculations of GW signals and event rates in this Section.

## 2.1 Cosmological Simulations

As reported in [Zhu et al. \(2020\)](#), we have performed a suite of 15 cosmological zoom-in simulations of the same host halo but with different BH seeds and accretion models to study the formation of  $z \sim 6$  quasars. We will use six of these simulations for the present study. Here we give a brief summary of the simulation, and refer to [Zhu et al. \(2020\)](#) for a more detailed description.

The simulations were carried out with the Lagrangian code GIZMO developed by [Hopkins \(2015\)](#), with the following physical processes implemented by [Zhu & Li \(2016\)](#): a multiphase ISM BSS: Define ISM model and the Schmidt-Kennicutt recipe for star formation ([Springel & Hernquist 2003](#)); a chaotic cold cloud accretion model for BHs; quasar mode feedback from accreting BHs; radiative and kinetic feedback from supernovae ([Springel et al. 2005](#)); metal-dependent radiative cooling and heating ([Wiersma et al. 2009](#)); and chemical enrichment from stellar evolution ([Vogelsberger et al. 2013](#)).

The unique features of these simulations important to this study include: three types of BH seeds in the mass range of  $10-10^6 M_\odot$ ; both thin-disk accretion with constant radiative efficiency and super-critical slim-disk accretion with varying radiative efficiency; and mergers of BH binaries in the cosmological context of galaxy formation and evolution.

The initial conditions of the zoom-in simulations focus on the most massive halo in a  $\sim 2.5 \text{ (Gpc)}^3$  volume, which has a mass of  $1.16 \times 10^{13} M_\odot$  at redshift  $z = 6.1$ . This galaxy has a number of major mergers at  $z > 6$ , and it was shown to reproduce several physical and panchromatic properties of distant quasars observed at  $z \sim 6$  ([Li et al. 2007](#); [Li et al. 2008](#); [Zhu et al. 2020](#)). The mass resolutions of the simulations are  $m_{\text{gas}} = 6.5 \times 10^5 M_\odot/h$ ,  $m_{\text{star}} = 6.5 \times 10^5 M_\odot/h$ ,  $m_{\text{DM}} = 3.5 \times 10^6 M_\odot/h$ , for gas, stars and dark matter particles, respectively, and the gravitational softening length is  $\epsilon = 0.5 \text{ kpc}/h$ . The simulations were run from  $z = 99$  to  $z = 6$  with the Planck cosmological parameters for a standard  $\Lambda$ CDM universe ([Planck Collaboration et al. 2016](#)):  $\Omega_M = 0.308$ ,  $\Omega_b = 0.048$ ,  $\Omega_\Lambda = 0.692$ ,  $h = 0.678$  and  $\sigma_8 = 0.82$ .

These simulations cannot directly resolve low-mass BHs ( $10-100 M_\odot$ ) formed from Pop III stars, but we used a novel technique to treat new BHs so that a fraction becomes a “ghost particle” attached to the BH and it interacts with other particles only by gravity. The BH particle has the same dynamics as its “ghost” while maintaining its own mass and accretion activity. This technique reduces potential numerical artifacts caused by the large mass difference between the small BHs and other particles, as demonstrated in [Zhu et al. \(2020\)](#).

In this study, we use six of the zoom-in simulations of [Zhu et al. \(2020\)](#), namely S1, S2, S3, S4, S5-REF, and S6, which were run with BH seeds with a mass of  $10, 10^2, 10^3, 10^4, 10^5, 10^6 M_\odot$ , respectively, as listed in Table 1 in [Zhu et al. \(2020\)](#). We extract the merging histories of the BHs and use the same cosmological parameters in the calculations of the GW signals from these mergers.

Figure 1 shows the BH mergers extracted from the six simulations. There are 29987, 5283, 78, 57, 60, 57 BH mergers from the simulations with BH seed mass of  $10^1, 10^2, 10^3, 10^4, 10^5, 10^6 M_\odot$ , respectively. There are more mergers in the S1 and S2 simulations than the rest, because the light seeds form from Pop III stars, which are abundant in the early evolution of the host galaxies, while in the case of intermediate and heavy seeds ( $10^3-10^6 M_\odot$ ), only one seed

forms in a halo above  $10^{10} M_\odot$ , which significantly limits the number of BH mergers. These BH mergers appear to have a wide range of mass ratios. In this work, we focus only on mergers occurring in the redshift range of  $z \sim 23-6$  to explore the GW signals from the early BBHs in the context of the formation of the first massive BHs and quasars.

### 2.1.1 Black Hole Seeds

In order to provide theoretical modeling for the GW detectors to search for BH seeds of the first quasars, we consider all three potential types of BH seeds in our model: light seeds of  $\sim 10^{1-2} M_\odot$ , intermediate mass seeds of  $\sim 10^{3-4} M_\odot$ , and heavy seeds of  $\sim 10^{5-6} M_\odot$ .

In our simulations, the light BH seeds ( $M_{\text{seed}} = 10-10^2 M_\odot$ ) form from Pop III stars when the stellar metallicity of  $Z$  is below a critical value of  $10^{-4} Z_\odot$ . We then convert a fraction of this particle into a BH particle of either  $M_{\text{seed}} = 10 M_\odot$  (S1 simulation) or  $M_{\text{seed}} = 10^2 M_\odot$  (S2 simulation). The parent star particle then becomes a “ghost particle” attached to the new BH. The BH has the same dynamics as its “ghost” parent particle while maintaining its own mass and accretion activity.

For the intermediate ( $M_{\text{seed}} = 10^3-10^4 M_\odot$ ) and heavy seeds ( $M_{\text{seed}} = 10^5-10^6 M_\odot$ ), owing to the uncertain formation conditions, we adopt a simplified scheme commonly used in cosmological simulations to plant the seeds of  $10^3, 10^4, 10^5, 10^6 M_\odot$ , respectively, in the center of a galaxy halo when its mass reaches  $M_{200} = 10^{10} M_\odot$ , as in the S3, S4, S5-REF, and S6 simulations, respectively ([Zhu et al. 2020](#)).

### 2.1.2 Black Hole Mergers

In a BBH system, the BH pair orbit each other slowly and emit weak GWs. As the emitted radiation carries away energy and angular momentum from the system, the orbit decays as a result of radiation reaction until the BHs eventually merge and settle down into a single stationary Kerr BH.

The no-hair and uniqueness theorems in GR state that a BH in its final stationary vacuum state can be completely characterized by three observable classical parameters: mass, electric charge and spin ([Israel 1968](#)). BSS: Astrophysical BHs are considered to be electrically neutral, therefore, each coalescing BBH pair can be fully characterized by the following parameters: masses of each BH,  $m_1$  and  $m_2$  and their spin angular momenta  $\vec{S}_1$  and  $\vec{S}_2$ . For simplicity, we will assume that the BH spins are aligned with the angular momentum; in this case we need only consider the dimensionless magnitudes of their spin:  $\chi_{1,2} \equiv c|\vec{S}_{1,2}|/(Gm_{1,2}^2)$ . We will assume that BHs are in quasi-circular orbit by the time they enter the LISA and 3G in which case the only other parameter needed is the GW frequency  $f$ . In addition to these intrinsic parameters, it is necessary to also specify the luminosity distance of the binary and the four angles defining the orientation of the orbit with respect to the line-of-sight ( $\psi, i$ ) and the position of the source in the sky ( $\alpha, \delta$ ). The luminosity distance can be computed from the source’s redshift. The signal-to-noise ratio critically depends on the angles which we would not know ahead of time. We will, therefore, compute the signal-to-noise ratio for each source by averaging over all angles as enumerated in Section 3.

The characteristic gravitational waveform generated from the resulting BBH merger depends on the mass ratio, spin and distance of the BBH system. The initial orbital period must be  $\leq 0.3$  days

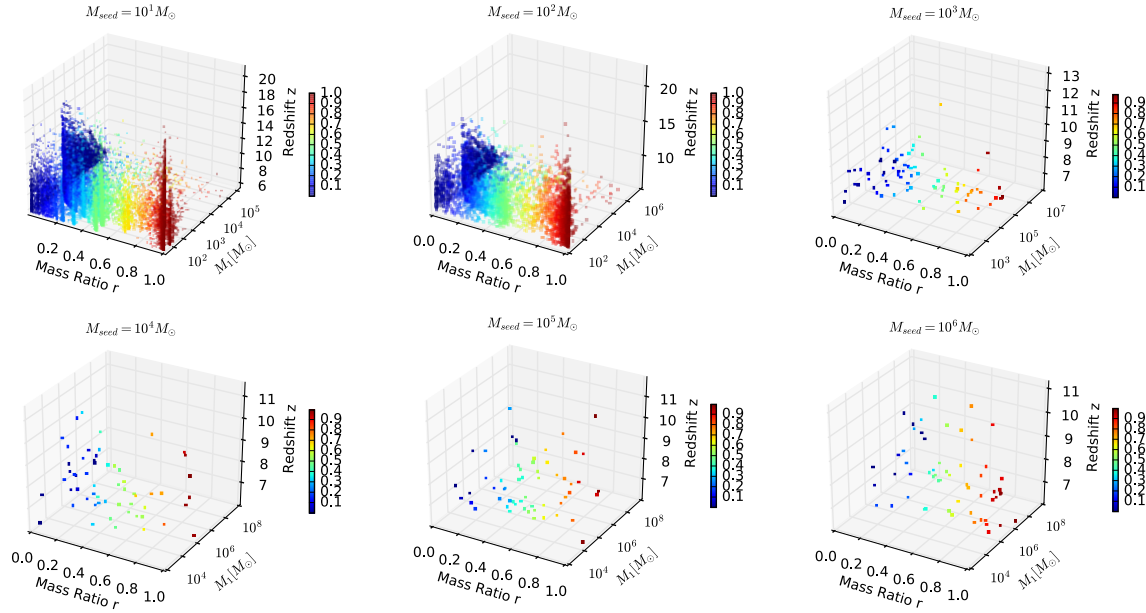


**Figure 1.** Black hole mergers extracted from the six simulations with BH seed mass of  $10^1, 10^2, 10^3, 10^4, 10^5, 10^6 M_\odot$ , respectively. Each panel shows the mass of the primary BH, the mass ratio, and the redshift of all the mergers. The colored dots represent the merger event, color-coded by the mass ratio as indicated by the color bar.

$(M/M_\odot)^{5/8}$  for gravitational radiation reaction to drive the binary to merge within a Hubble time (Shapiro & Teukolsky 1983). This means that for stellar-mass BHs ( $\leq 100 M_\odot$ ), the orbital period is on the order of seconds to days, while for SMBHs ( $10^6 - 10^9 M_\odot$ ) on the order of years to hundreds of years. The BH merging process can be divided into three phases:

- **Inspiral Phase:** the slow, adiabatic inspiral phase is driven by gravitational radiation damping on a timescale much longer than the orbital period. The binary's orbit gradually decays as a result of energy and angular momentum losses as the binary begins to slowly inspiral. The inspiral phase ends when the separation of the BHs approaches the innermost stable circular orbit (ISCO) at radius  $r_{\text{ISCO}} > 6 GM/c^2$ ,  $M = m_1 + m_2$ . During this phase, post-Newtonian expansions are used to approximate the dynamics and gravitational waveforms of the binary (Blanchet 2014).
- **Merger Phase:** the non-adiabatic, highly non-linear merger phase begins when the BH pair reaches its maximum orbital frequency (i.e. the frequency at the ISCO or the merger frequency  $f_{\text{ISCO}}$ ), or equivalently, when the radiation-reaction timescale reaches the orbital period. The separation of the binary approaches the radius of the innermost stable circular orbit ( $\leq r_{\text{ISCO}}$ ) and continues to decrease rapidly as the BHs undergo a freely-falling plunge toward each other. The transition from the adiabatic inspiral, driven by radiation-reaction, to an unstable plunge, induced by strong space-time curvature, is expected to occur for orbits more tightly bound than the innermost stable circular orbit in a Schwarzschild metric of mass (Buonanno & Damour 1999). To fully describe the merger gravitational waveforms, a complete machinery of general relativity is needed, and this can only be achieved by Numerical Relativity

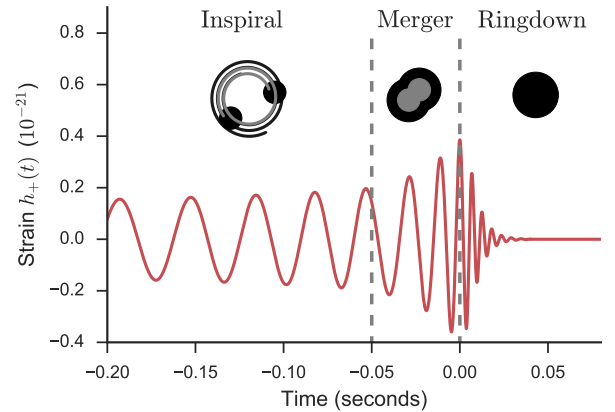


**Figure 2.** A schematic diagram of the time-domain full inspiral-merger-ringdown gravitational waveform for a non-spinning, equal-mass ( $10 M_\odot$ ) BBH coalescence. This is a hybrid waveform matched smoothly to post-Newtonian inspiral signal. The plus polarization of the dimensionless strain amplitude,  $h_+(t)$  is plotted against time for the dominant ( $l = 2, m = 2$ ) spin-weighted spherical harmonic mode. The vertical dashed lines roughly separate the inspiral, merger and ringdown phases.

(NR). Buonanno & Damour (1999) were able to extend the evolution through the plunge phase by an approach called the Effective One-Body formalism which defines, in a non-perturbative manner, the late dynamical evolution of a coalescing binary system.

- **Ringdown Phase:** the quasi-normal ringdown phase, during which



the system evolves towards its quiescent state, and the resulting BH settles down to a rotating Kerr BH, emitting GWs due to deviations from the final axisymmetric state. The dynamics of the ringdown phase, though non-linear, can be accurately described as oscillations of the final BH's quasinormal modes using perturbation theory on the Kerr spacetime background (Vishveshwara 1970). The perturbation theory in which the Einstein field equations are expanded around the BH metric in powers of the mass ratio  $m_2/m_1$  can be used to describe the motion and radiation of a small body around a large body. One needs to develop a consistent framework free of divergences within the gravitational self-force formalism in order to account for back-reaction of the gravitational field of the smaller body on itself (Buonanno & Sathyaprakash 2014). The corresponding GWs from the ringdown are described by a superposition of exponentially damped sinusoids that are most strongly dominated by the  $l = 2, m = 2$ , quasi-normal mode.

Figure 2 illustrates the evolution of the three phases from inspiral to merger to ringdown of a non-spinning equal stellar-mass ( $10M_\odot$ ) BBH merger.

### 2.1.3 Treatment of the Inspiral and Merger Phases for the BBHs from the Cosmological Simulations

In the cosmological simulations, a BBH forms when two BHs become gravitationally bound, or in the case of galaxy mergers, when the massive BHs in the center of the galaxy progenitors sink through the potential well through dynamical friction to form a bound binary. Due to limited resolution in the simulations, we cannot resolve the innermost stable circular orbit  $r_{\text{isco}}$ , so the BH binaries are assumed to merge when the separation of the pair is below the spatial resolution of 0.5 kpc/h (Zhu et al. 2020). Here we adopt a similar approach as in other studies (e.g., Salcido et al. 2016; Kelley et al. 2017, 2018; Siwek et al. 2020; Volonteri et al. 2020) to treat the inspiral and merger phases. We assume that the inspiral phase starts when the BBH is within the spatial resolution, and the inspiral timescale is calculated as follows.

In the Newtonian limit, the orbital radius  $r$  and orbital angular velocity  $\Omega$  are linked by the Keplerian relation<sup>1</sup>:

$$\frac{M}{r} \equiv \frac{1}{\tilde{r}} \equiv (M\Omega)^{2/3} \equiv \tilde{\Omega}^{2/3} \quad (1)$$

where  $\tilde{r}$  and  $\tilde{\Omega}$  are the dimensionless radius of the orbit and the dimensionless orbital angular velocity, respectively.

The gravitational wave frequency in harmonic  $m$  is given by

$$f_m = \frac{m}{2\pi M} \tilde{\Omega} \quad (2)$$

We only consider the dominant  $m = 2$  mode for which the corresponding frequency is:

$$f_2 = \frac{\Omega}{\pi} \quad (3)$$

The total time duration of the inspiral phase until ISCO is reached,  $T_{\text{insp}}$ , is given, in the limit  $m_2 \gg m_1$  by (Sathyaprakash &

Dhurandhar 1991):

$$\begin{aligned} T_{\text{insp}} &= \frac{5}{256} \frac{1}{\eta} \frac{M}{\tilde{\Omega}^{8/3}} \tau \\ &= 1.41 \times 10^6 \text{ sec} \left( \frac{f_2}{10 \text{ mHz}} \right)^{-8/3} \left( \frac{10M_\odot}{m_1} \right) \left( \frac{10^6 M_\odot}{M} \right)^{2/3} \tau \\ &= 0.141 \text{ sec} \left( \frac{f_2}{100 \text{ Hz}} \right)^{-8/3} \left( \frac{10M_\odot}{m_1} \right) \left( \frac{100M_\odot}{M} \right)^{2/3} \tau \end{aligned} \quad (4)$$

where  $\eta = m_1 m_2 / M^2$  is the symmetric mass ratio,  $M$  is the total mass, and  $\tau$  is the relativistic correction to  $T_{\text{insp}}$  which is a function of the orbital radius  $r/r_{\text{isco}}$  and BH spin parameter as given in Table IX of Finn & Thorne (2000). BSS: Please note that the above approximation is only valid if  $m_2 \gg m_1$  and so doesn't quite apply to the second case. However, there is no need to make this approximation. Also, I get inspiral times that are very different from the ones quoted above; I will liaise with Yiting to get correct this.

The parameter  $r/r_{\text{isco}}$  can be expressed as a ratio of  $f_2$  and  $f_{\text{isco}}$  by solving Equations (2) and (3) simultaneously:

$$\frac{r}{r_{\text{isco}}} = \left( \frac{f}{f_{\text{isco}}} \right)^{-2/3} \quad (5)$$

The ISCO is at the location  $\tilde{r}_{\text{isco}}$  where the object's total energy  $E(\tilde{r})$  is a minimum, or equivalently, where the time derivative of  $\Omega$  is infinite.  $\tilde{r}_{\text{isco}}$  is the root of the quartic equation  $\tilde{r}^2 - 6\tilde{r} + 8\chi\tilde{r}^{1/2} - 3\chi^2 = 0$ , which lies between 1 (when  $\chi=1$ ) and 6 (when  $\chi=0$ ). Since the BH spin is assumed to be 0 in our analysis, the frequency at the ISCO is calculated as:

$$\begin{aligned} f_{2,\text{isco}} &= \frac{\Omega}{\pi} = \frac{\tilde{\Omega}_{\text{isco}}}{\pi M} \\ &= \left( \frac{1}{\tilde{r}_{\text{isco}}} \right)^{3/2} / \pi M \\ &= \frac{\tilde{r}_{\text{isco}}^{-3/2}}{M\pi} = \frac{6^{-3/2}}{M\pi} \end{aligned} \quad (6)$$

For each BBH extracted from the cosmological simulations, we add the timescale  $T_{\text{insp}}$  as the inspiral phase, after that the BBH is assumed to coalesce and reach the merger phase.

## 2.2 Gravitational Wave Calculations

For the BBHs extracted from the cosmological simulations, we apply a phenomenological gravitational waveform model to the merging pairs to calculate the GW amplitude, Signal-to-Noise ratio (SNR), and event rates of the systems.

### 2.2.1 Gravitational Wave Amplitude

To calculate the GW from BBHs, we adopt the following notation, along with the physical parameters of a BH binary,  $\Xi \in (M, \eta, \chi_1, \chi_2)$ , where  $M$  is the total mass of the BBH,  $\eta$  is the mass ratio, and  $\chi_1$  and  $\chi_2$  are the spin parameter of the BHs, respectively, defined as follows (assuming  $m_1 > m_2$ ):

$$\begin{aligned} M &= m_1 + m_2, \\ \eta &= \frac{m_2}{M}, \\ \chi_i &= \frac{\vec{S}_i \cdot \hat{L}}{m_i^2}. \end{aligned} \quad (7)$$

<sup>1</sup> BSS: Unless specified otherwise, we use the geometric system of units in which  $G = c = 1$ .

**Table 1.** A list of the GW detectors and relevant parameters considered in our study.

Detector	Generation	Country	Date	Arm length (km)	Frequency (Hz)	$f_0$ (Hz)	$S_n(f)$ or $S_n(x)$
Ground-based detectors							
aLIGO	First	USA	2015	4	$10 - 10^4$	500	$(x^{-4.14} - 5x^{-2} + \frac{111(1-x^2+0.5x^4)}{1+0.5x^2}) / (1.0 \times 10^{-49})$
ET-D	Third	Italy	2025	10	$1 - 10^4$	200	$(x^\alpha + a_0x^\beta + \frac{b_0(1+b_1x+b_2x^2+b_3x^3+b_4x^4+b_5x^5+b_6x^6)}{1+c_1x+c_2x^2+c_3x^3+c_4x^4}) / (1.5 \times 10^{-52})$
CE	Third	USA/Australia	–	40	$8 - 300$	–	$5.77 \times 10^{-31} / f^{20} + 4.89 \times 10^{-45} / f^4 + 1.1 \times 10^{-50} + 2.00 \times 10^{-55} f^2$
Space-based detectors							
LISA	Third	Europe	2034	$5 \times 10^6$	$3 \times 10^{-5} - 1$	$10^{-3}$	$(\sqrt{10}x^{-14/3} + 1 + x^2/1000 + 313.5x^{-(6.398+3.518\log 10x)}) \times (4.2 \times 10^{-41})$
BBO	Third	Europe	–	$5 \times 10^4$	$10^{-3} - 10$	–	$2.00 \times 10^{-49} f^2 + 4.58 \times 10^{-49} + 1.26 \times 10^{-52} f^{-4}$
DECIGO	Third	Japan	2027	$10^3$	$0.1 - 10$	7.36	$7.05 \times 10^{-48} [1 + (f/f_0)^2] + 4.8 \times 10^{-51} f^{-4} \frac{1}{1+(f/f_0)^2} + 5.33 \times 10^{-52} f^{-4}$

Notes: (1) Detector name. (2) Generation. (3) Country. (4) Expected commissioning date. (5) Interferometer arm length. (6) Frequency range. (7) The reference frequency  $f_0$ . (8) The approximated analytical noise spectral density in either  $S_n(f)$  as in Eqn. (12), or  $S_n(x)$ , where  $x$  is dimensionless frequency  $x = f/f_0$ . The parameters for ET-D are  $\alpha = -4.1, \beta = -0.69, \alpha_0 = 186, \beta_0 = 233, \beta_1 = 31, \beta_2 = -65, \beta_3 = 52, \beta_4 = -42, \beta_5 = 10, \beta_6 = 12, c_1 = 14, c_2 = -37, c_3 = 19, c_4 = 27$ .

where  $\chi_i \in [-1, 1]$ , and the BH spin angular momenta  $\vec{S}_i$  are assumed to be parallel to the direction of the orbital angular momentum,  $\hat{L}$ .

The GW amplitudes are often expressed in the Fourier domain. The commonly used frequency-domain phenomenological model, the “PhenomD” model (Husa et al. 2016), is adopted in our study to calculate the Fourier amplitude of GWs from the Inspiral and Merger-Ringdown phases of non-precessing BBH systems with aligned spins. The “PhenomD” model is a hybrid waveform model that combines the uncalibrated analytical effective-one-body (EOB) model with NR simulation data designed to provide waveform templates for the dominant spherical harmonic modes ( $l = 2, |m| = 2$ ) of the GW signals. The Inspiral regime is modeled by the uncalibrated EOB model from a minimum frequency up to the transition frequency  $f_{\text{isco}}$  at which the model switches to NR simulations. Beyond the Inspiral regime at frequencies greater than the transition frequency, the “PhenomD” model is calibrated against NR data to model the Merger-Ringdown waveforms. Within the calibration range of “PhenomD” model (mass ratio up to 1 : 18 and spin up to  $|\chi| \sim 0.85$  for aligned-spin BBHs), it is proven to be the most accurate waveform model for signal detection and waveform modeling, losing less than 0.5% of the recoverable S/N, among its most recent counterparts (Kumar et al. 2016).

The GW signal  $h(t)$  can be described by a linear combination of two independent orthogonal polarization components:  $h_+$  and  $h_\times$ . The response of the detector to an incoming gravitational wave depends on the detector geometry. The expression for the dominant spherical-harmonic modes of the GW signal in terms of the physical parameters  $\Xi \in (M, \eta, \chi_1, \chi_2)$  (Eqn. 7) and the observer’s orientation  $(\theta, \phi)$  with respect to the orbital angular momentum of the binary is given by Husa et al. (2016):

$$\begin{aligned} \tilde{h}(f; \Xi, \theta, \phi) &= \tilde{h}_+(f; \Xi, \theta, \phi) - i\tilde{h}_\times(f; \Xi, \theta, \phi) \\ &= \sum_{m=-2,2} \tilde{h}_{2m}(f; \Xi)^{-2} Y_{2m}(\theta, \phi) \end{aligned} \quad (8)$$

And the full Inspiral-Merger-Ringdown (full IMR) frequency domain waveform in the spherical harmonic mode is:

$$\tilde{h}_2(f; \Xi, \theta, \phi) = A(f; \Xi) e^{i\phi(f; \Xi)} \quad (9)$$

Consider only the real part of the signal which carries physical meaning, the Fourier-domain signal in “PhenomD” model can be

generated via

$$\tilde{h}_+(f; \Xi, \theta, \phi) = |\tilde{h}_+(f; \Xi, \theta, \phi)| \text{Re}[e^{i\phi(f; \Xi)}] \quad (10)$$

In addition to the intrinsic properties  $\Xi \in (M, \eta, \chi_1, \chi_2)$  of a BBH system and its orientation with respect to the orbital angular momentum, the amplitude of the gravitational wave signal from such a system is also a function of luminosity distance  $d_L$ . The luminosity distance – redshift relation in a perturbed Friedmann–Robertson–Walker Universe being the background matter-dominated Universe is given by (Barausse et al. 2005):

$$d_L = \frac{c}{H_0} [z + \frac{z^2}{2}(1 - q_0) + O(z^3)] \quad (11)$$

where  $H_0$  is the unperturbed Hubble constant and  $q_0$  is the unperturbed deceleration parameter.

### 2.2.2 Detector Sensitivity

The sensitivity of a GW detector is often described by the root power spectral density (PSD),  $\sqrt{S_n(f)}$ , and the spectral energy density  $\Omega_{\text{GW}} h_{100}^2$ . In contrast, the amplitude of a GW source can be expressed by the characteristic strain. The root PSD that describes the strain noise is given by (Moore et al. 2015):

$$\sqrt{S_n(f)} = h_n(f) f^{-\frac{1}{2}} \quad (12)$$

where the detector noise curve  $S_n(f)$ , can be obtained from analytical fits or interpolation to the sensitivity data.

For this study, we select three ground-based detectors aLIGO, ET-D (the high-sensitivity configuration of ET), and CE, and three space-borne interferometers LISA, BBO, and DECIGO. The sensitivity of ground-based GW detectors is affected by the time-varying local gravitational field induced by numerous noise sources such as low frequency seismic vibrations, density variation in the atmosphere due to winds, etc. Below a certain frequency cutoff, the noise PSD is assumed to be infinite (Sathyaprakash & Schutz 2009). Space-based detectors are more sensitive to lower frequency GWs compared to ground-based detectors. This is because space-based detectors can have much longer arms and are unaffected by seismic noise, which limits the low frequency performance of ground-based detectors. The canonical design for a space-based detector is LISA, consisting of three satellites flying in a triangular constellation in a 1AU orbit around the sun (Sathyaprakash & Schutz 2009). More

ambitious proposals such as third-generation space- detectors BBO and DECIGO are designed to probe decihertz GWs.

In Table 1, we list the GW detectors considered in this study, and summarize the analytical approximations of the PSD for each detector. For aLIGO, ET-D, and LISA, the PSD is expressed in terms of a dimensionless frequency as  $S_n(x)$ , where  $x = f/f_0$ , and  $f_0$  is a fixed reference frequency for a given detector. For LISA, we adopt the analytical fits given by [Scharre & Will \(2002\)](#) which include the LISA instrumental noise and an estimate of “confusion noise” from a population of galactic white-dwarf binaries. The analytical approximations of the BBO and DECIGO noise curves are given by [Yagi & Seto \(2011\)](#), where the first, second and third terms in the DECIGO/BBO sensitivity curve represent the shot noise, the radiation pressure noise and the acceleration noise, respectively.

**In this study, we will also consider the newly proposed three-detector-network “3G” that combines CE and ET ([Schutz & Sathyaprakash 2020](#)), and provide predictions for it.**

### 3 RESULTS

We applied the “PhenomD” model to six cosmological zoom-in simulations of the first quasars in [Zhu et al. \(2020\)](#) to calculate the GW signals from the BBH mergers in the early Universe. In this Section, we report four main results: (i) The characteristic strain amplitudes from BH mergers in the simulations. (ii) The Signal-to-Noise Ratios (SNRs) of the Inspiral and Merger-Ringdown sources. (iii) The predictions of event rates for ground-based and space-based detectors. (iv) The redshift distributions for all the resolvable merger events during the assembly of the first quasars in the simulations.

#### 3.1 Gravitational Wave Characteristic Strain from Black Hole Seeds of the First Quasars

When a GW passes a detector, the fractional change induced in the arm lengths of the detector will be recorded as a dimensionless strain as a function of time,

$$h(t) = \frac{\Delta L(t)}{L} \quad (13)$$

The characteristic strain is designed to incorporate the effect of integrating an inspiralling signal ([Moore et al. 2015](#)). The characteristic strain amplitude of the GW sources is defined as:

$$h_c(f) = 4f^2 |\tilde{h}(f)|^2 \quad (14)$$

where  $f$  is the rest-frame frequency of the source and  $\tilde{h}(f)$  is the Fourier transform of the strain signal given by

$$\tilde{h}(f) = \mathcal{F}\{h(t)\}(f) = \int_{-\infty}^{\infty} h(t) e^{-2\pi i f t} \quad (15)$$

Similarly, the characteristic noise strain of GW detectors can be obtained by rearranging Eqn. (12),

$$[h_n(f)] = \sqrt{S_n(f)} f^{\frac{1}{2}} \quad (16)$$

where  $S_n(f)$  is the analytical approximation of the noise spectral densities listed in Table 1.

We follow the approach of [Salcido et al. \(2016\)](#) to calculate  $h_c(f)$  and  $h_n(f)$  from our simulations in the following steps :

1. Extract the merger tree of each BH seed from the simulation and derive the intrinsic parameters of each merging BBH pair at the time of “merger” at a certain redshift (i.e. the merger redshift).

2. The coalescence process is divided into inspiral and merger-ringdown phases following the method outlined in Section 2.1.3. The inspiral phase starts when the distance between the BBH pair is below the spatial resolution, and it lasts for a duration  $T_{\text{insp}}$  (Eqn. 4), after that the pair coalesces and enters the merger-ringdown phase.
3. Compute the frequency at merger (i.e. the merger frequency)  $f_{\text{isco}}$  using Eqn. (6), and convert it to the observed frequency as  $f_{\text{obs}} = f_{\text{isco}}/(1+z)$ .
4. Use the “PhenomD” model to compute the frequency-domain amplitudes of the GW signals,  $|\tilde{h}(f_{\text{obs}})|$ , from all the BH coalescence events in each simulation, assuming no BH spin.
5. Calculate the characteristic strain amplitude at the observed merger frequency  $h_c(f_{\text{obs}})$  using Eqn. (14).
6. Calculate the characteristic noise amplitude at the observed merger frequency  $h_n(f_{\text{obs}})$  of each GW detector using Eqn. (16).
7. Use the “PhenomD” model to compute the theoretical predictions of  $h_c(f)$  from equal-mass, non-spin BBH systems for masses from  $M_1 = M_2 = 10^1 M_\odot$  to  $M_1 = M_2 = 10^9 M_\odot$ , and for redshifts  $z \approx 25 - 0.001$ .

The resulting GW characteristic strain amplitudes  $h_c(f_{\text{obs}})$  for all BBH mergers at different redshifts from the six cosmological zoom-in simulations of [Zhu et al. \(2020\)](#) are shown in Figure 3, in comparison with the theoretical predictions of equal-mass mergers at different redshifts, and with sensitivity curves of GW detectors aLIGO, ET-D, CE, LISA, and BBO. Since BBO and DECIGO are similar to decihertz space antennae that probe the decihertz frequency band ( $10^{-2}$  to 10 Hz), we only show the BBO curve in the plots for simplicity, and we refer readers to [Schmitz \(2020\)](#) for DECIGO’s sensitivity curve. Note that in this Figure we plot only the  $h_c(f_{\text{obs}})$  of the Merger-Ringdown phase for illustration purpose. The results of the Inspiral phase will be presented in the next sections.

Figure 3 shows a trend that the characteristic strain amplitude increases as the masses of the BH mergers increase, with decreased observed frequency. There are a large number of BH mergers from stellar-mass seeds ( $10 - 10^2 M_\odot$ ) because these seeds formed from numerous PopIII stars, while for heavy seeds ( $10^3 - 10^6 M_\odot$ ) only one BH formed in a halo above  $10^{10} M_\odot$ , so there are only a few mergers in the simulations.

For the  $M_{\text{seed}} = 10^1 M_\odot$  simulation (top left panel), the mergers of  $\sim 10 M_\odot$  BHs first occur at high redshift  $z \sim 21$ , which have  $h_c(f_{\text{obs}}) \sim 10^{-23} - 10^{-22}$  in the frequency of 1 – 10 Hz, may be marginally detectable by ET-D and CE. Both detectors can also detect similar low-mass mergers occurring at lower redshifts down to  $z \sim 6$ . As the BHs grow to be more massive, the mergers shift to lower frequencies in the regime of space-based GW interferometers. BBO can detect BH mergers of  $10^2 - 10^4 M_\odot$  in the redshift range  $z \sim 6 - 21$ , while LISA can detect mergers of  $\sim 10^4 M_\odot$  out to  $z \sim 15$  (top middle and right panels). For massive BH mergers of  $\gtrsim 10^5 - 10^6 M_\odot$ , they populate a  $h_c - f_{\text{obs}}$  space that can be detected by LISA in the redshift range  $z \sim 12 - 6$  (bottom panels), but for more massive mergers of  $\geq 10^7 M_\odot$ , they move out of LISA’s frequency range and into the regime of the Pulsar Timing Array (not shown here). The signals of the massive BBHs in Figure 3 are in good agreement with those of [Salcido et al. \(2016\)](#).

These results demonstrate that a combination of the third-generation ground- and space-based GW detectors will provide an extremely powerful tool to study BH mergers of a wide range of masses of  $10^1 - 10^7 M_\odot$  and in unprecedented redshift range of  $z \sim 21 - 6$ , which is critical for solving the outstanding questions of the BH seeds and the assembly of the first SMBHs.

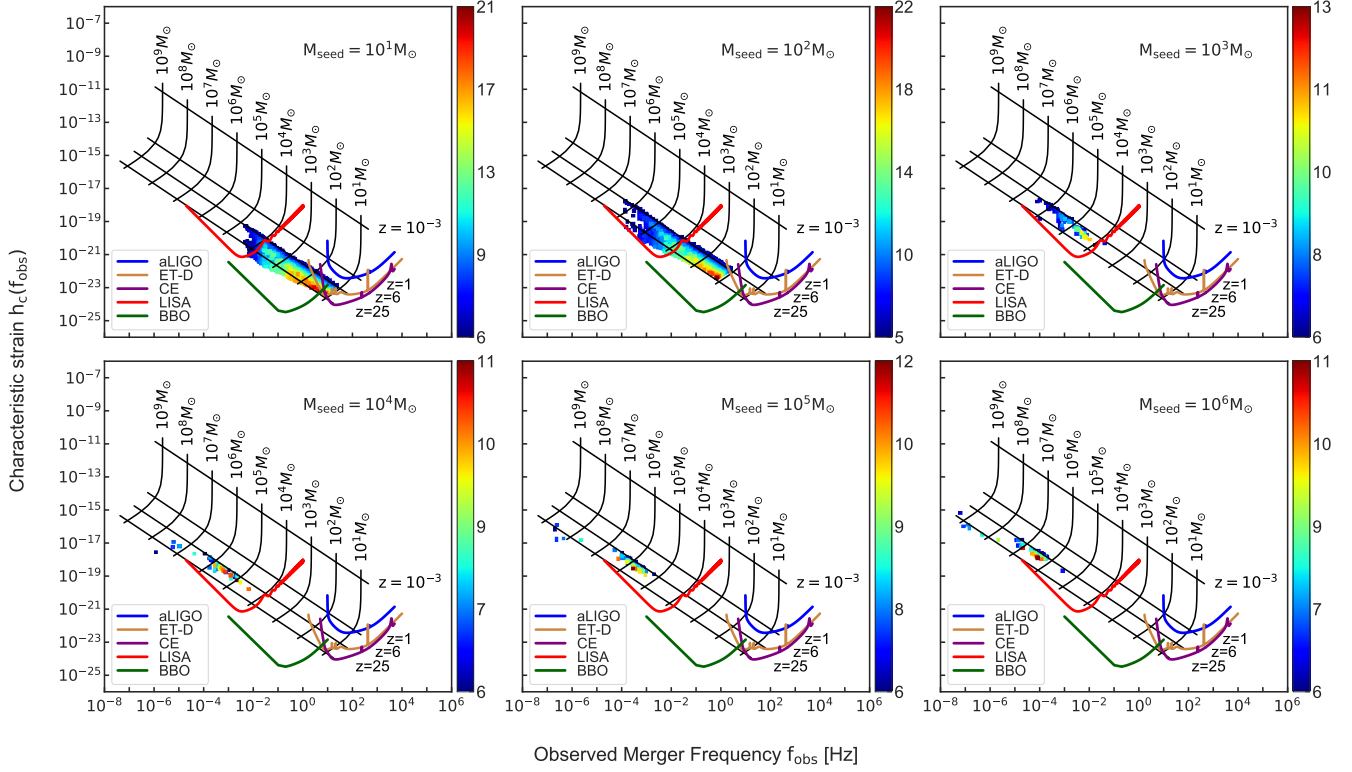


**Figure 3.** The gravitational wave characteristic strain amplitude  $h_c(f_{\text{obs}})$  of the Merger-Ringdown Phase as a function of observed merger frequency for all the BBH coalescences from the six simulations of [Zhu et al. \(2020\)](#) with BH seed of  $10^1, 10^2, 10^3, 10^4, 10^5, 10^6 M_\odot$ , respectively. The observed merger frequency is the transition frequency between Inspiral and Merger-Ringdown phase at the ISCO  $f_{\text{obs,ISCO}} = (6^{-3/2})/(\pi M)$ . The masses used here are the redshifted masses  $M = M(1+z)$ . In each of the panels, the colored points are the BH merger events in the simulations color-coded by the redshift at time of merger, in comparison with the sensitivity curves of ground-based detectors aLIGO, ET-D, CE and space-based detectors LISA, BBO, while the black grid lines represent the theoretical predictions of  $h_c$  from equal-mass, non-spin BBH mergers from  $M_1 = M_2 = 10^1 M_\odot$  to  $M_1 = M_2 = 10^9 M_\odot$  at redshifts  $z = 0.001, 1, 6, 25$ , respectively, for reference purpose. The  $h_c$  data above a detector sensitivity curve is regarded as a resolvable event by the instrument.

### 3.2 Detectability of Black Hole Mergers During the Assembly of the First Quasars

A GW detector outputs a signal which is a linear superposition of noise characterized by the noise PSD  $S_n(f)$  and a potential GW signal:  $s(t) = n(t) + h(t)$ . To extract the GW signal from the detector output, a matched filtering technique is often used, which involves the construction of a Wiener optimal filter or a matched filter ([Moore et al. 2015](#)). The contributions from the signal and the noise can be separated by the convolution of the filter function of the Wiener filter with the detector output. Therefore, a complete family of theoretical waveform templates are needed from NR models prior to the matched filter search. In our calculation of the root-mean-square value of SNR,  $\rho_{\text{rms}}$ , we adopt the matched-filtering technique. The sky-averaged squared  $\rho_{\text{rms}}$  for a matched filter detection is related to the PSD of the noise in the detector as:

$$\rho_{\text{rms}}^2 = 4 \int_0^\infty \frac{|\tilde{h}(f)|^2}{S_n(f)} df \quad (17)$$

where  $\tilde{h}(f) = \int_{-\infty}^\infty e^{2\pi i f t} h(t) dt$  is the Fourier transform of the dimensionless strain  $h(t)$  produced from the “PhenomD” model.

Although the magnitude of the Fourier domain amplitude quantifies the amplitude of the GWs as a function of frequency, there is one disadvantage. For an inspiralling source, the amplitude at one instant during the inspiral epoch might be orders of magnitude below the noise level in a detector, but as the signal continues

over many orbits, the SNRs can be accumulated up to a detectable level ([Moore et al. 2015](#)). Thus, the formula given for the  $\rho_{\text{rms}}$  in Eqn. (17) no longer applies to the monochromatic inspiral source in this case. Here is where the characteristic strain comes into play. It is designed to include the effect of integrating an inspiral signal as the inspiralling binaries spend a variable amount of time in each frequency band. The precise definition of the characteristic strain  $h_c$  comes from the definition of the SNR ([Flanagan & Hughes 1998](#)):

$$\rho_{\text{rms}} = \sqrt{\int \left( \frac{h_{c,m}(f_m)}{h_n(f_m)} \right)^2 d\ln(f_m)} \quad (18)$$

where  $f_m$  is the GW frequency for harmonic mode  $m$  (Eqn. 2),  $h_c$  is the characteristic amplitude of the source (Eqn. 14), and  $h_n$  is the characteristic noise amplitude of the detector (Eqn. 16).

We follow the method in the review by [Finn & Thorne \(2000\)](#) to calculate the SNR value  $\rho$ . First, we need to determine the integration limits. For the inspiral signals in this work, we focus on the GWs generated from the final year of the inspiral phase, which is of great interest for probing the spacetime geometries of massive BHs ([Finn & Thorne 2000](#)). The lower limit of the integration is then obtained by setting  $T_{\text{insp}}$ , the time duration of the inspiral, to 1 year and finding  $f_2$ . This can be achieved by first performing a cubic interpolation to the data in Table IX of ([Finn & Thorne 2000](#)) to determine the analytical formula for the relativistic time correction



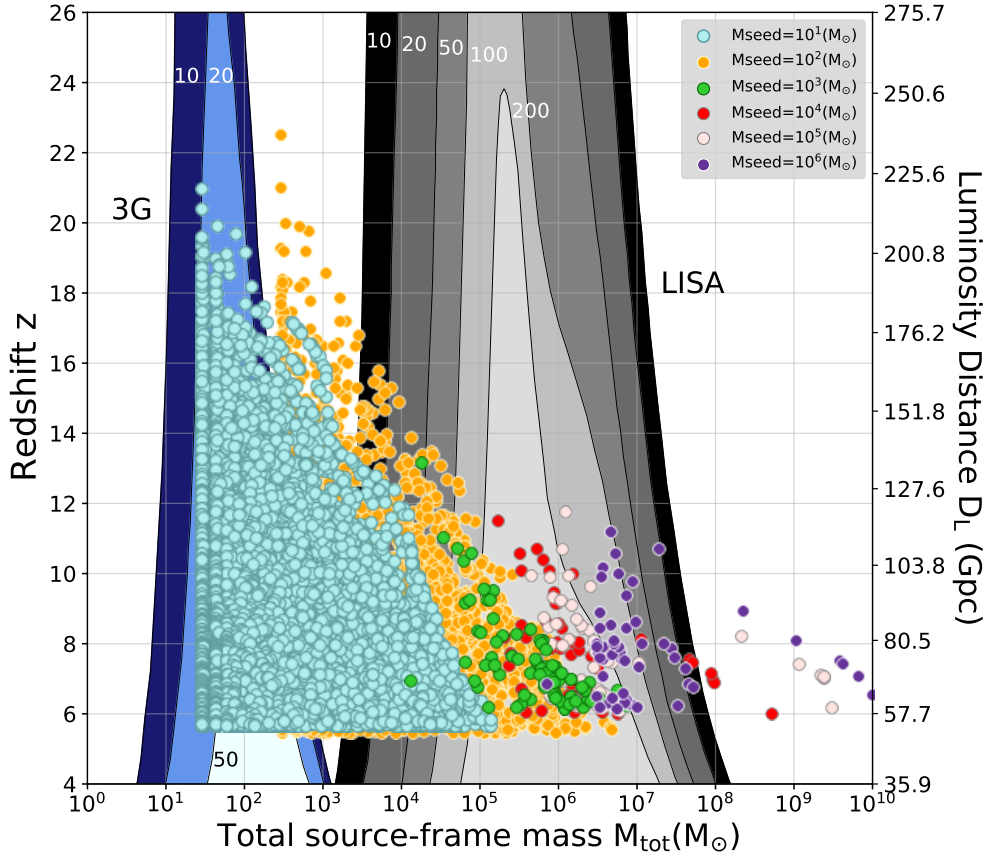


Figure 4. Distribution of the BBH coalescence events from six simulations in the  $M_{\text{tot}} - z$  plane, in comparison with the contours of constant SNRs for the “3G” network (blue contours) and LISA (grey contours), respectively. The colored points are BBH mergers from the zoom-in simulations with different BH seeds with SNRs above 10. Note that the contours are calculated for equal-mass BH binaries, which differ slightly from unequal-mass mergers, thus points that lie outside of the contours may be unequal-mass mergers that still meet the detection criteria.

function, and then using a simple root solver to find the frequency at time  $T = 1$  year. The upper limit of the integration is the frequency at the ISCO,  $f_{\text{isco}}$  (Eqn. 6). Once we have the integration limits, it is straightforward to compute  $\rho_{\text{rms}}$  for an inspiral source from Eqn. (18). We adopt geometric units  $G = c = 1$  in our calculations.

For the Merger-Ringdown phase, we adopt a maximum frequency of  $\infty$  as the upper limit of integration in Eqn. (17). For the lower limit, we set it to be the frequency at the beginning of the merger phase i.e.  $f_{\text{isco}}$  (Eqn. 6). The squared value of SNR for the Merger-Ringdown phase can then be expressed as:

$$\rho^2 = 4 \int_{f_{\text{isco}}}^{\infty} \frac{|\tilde{h}(f)|^2}{S_n(f_{\text{obs}})} df_{\text{obs}} \quad (19)$$

Due to the limited knowledge we have on the distribution and orientation of the sources in the sky plane with respect to the detectors, sources with high SNR values can sometimes avoid detection by a single detector depending on the inclination and orientation of the orbits of the BBHs (Sathyaprakash & Schutz 2009). In order to avoid potential “blind spots” and maximize the detection potential of the detectors, Schutz & Sathyaprakash (2020) proposed the 3-detector-network “3G”, which contains ET-D and two detectors of CE. Following Schutz & Sathyaprakash (2020), we use a crude approximation to estimate the total SNR of the “3G” network  $\rho_{3G}$  as a non-linear combination of those of CE ( $\rho_{\text{CE}}$ ) and ET ( $\rho_{\text{ET}}$ ), as given below:

$$\rho_{3G} = \sqrt{2\rho_{\text{CE}}^2 + \rho_{\text{ET-D}}^2} / 2.266 \quad (20)$$

Figure 4 shows the distribution of the BBH coalescence events from the six cosmological zoom-in simulations of different BH seeds in the total mass – redshift plane, in comparison with the sky-averaged constant SNR contours of equal-mass mergers for “3G” network and LISA, respectively. Such a figure is often called a “Waterfall” plot for GW detectors in reference of the shape of the contours. The colored circles represent the sources from different simulations. Points that fall within the detection limit with a SNR  $\rho = 10$  for each detector shall be detected. Note, however, that since the contours are for equal-mass BH mergers are slightly different from those of unequal-mass mergers, some sources outside of the contours may be unequal-mass BH mergers that still meet the detection criteria of the instruments and thus be detectable YL: (Katz & Larson 2018).

It is clear from Figure 4 that the “3G” network and LISA can detect the coalescences of BBHs of  $\sim 10^1 - 10^3 M_{\odot}$  and  $\sim 10^3 - 10^7 M_{\odot}$ , respectively, beyond redshift  $z \sim 30$  when the first dark matter halos collapse to form primordial galaxies. If massive Pop III stars form in these mini halos, they may leave behind BH seeds of  $\sim 10^1 - 10^2 M_{\odot}$ , or if some of the primordial galaxies collapse to form massive DCBHs before the onset of intense star formation, then the subsequent evolution of these seed BHs may be detectable by the “3G” network and LISA.

This is a significant improvement over the Advanced LIGO – Virgo network, which detected the most distant event to date, GW190521, from a luminosity distance of  $5300^{+2400}_{-2600}$  Mpc and a corresponding redshift of only  $z \sim 0.8$  (Abbott et al. 2020b).

In our simulations, a large number of BBHs from seeds of  $10^1 - 10^2 M_\odot$  from  $z \sim 21 - 6$  fall in the locus of “3G”, while most of those from seeds of  $10^3 - 10^6 M_\odot$  are detectable by LISA with high SNRs up to  $z \sim 16$ . These results are in good agreement with those of Valiante et al. (2020) from semi-analytical calculations.

As demonstrated in Figure 4, the unique capability of “3G” and LISA will cover the wide mass range of  $10^1 - 10^6 M_\odot$  for BH seeds from the theoretical models. Therefore, a synergy between the “3G” network and LISA will be able to provide a definitive answer to the origin of the first SMBHs at the cosmic dawn.

### 3.3 Event Rate of Black Hole Mergers at High Redshifts

The number of resolvable sources above the detection limit  $\text{SNR} = 10$  per redshift interval from  $z$  to  $z + dz$  is defined as  $\bar{N}(z, \text{SNR} \geq 10)/\Delta z V_c \sim d^2 \bar{n}(z, \text{SNR} \geq 10)/dz dV_c$ , where  $V_c$  is the co-moving volume. The estimated event rate of detected GW sources per observed time, integrating over all redshifts is given by Koushiappas & Zentner (2006):

$$\frac{d\bar{N}}{dt_{\text{obs}}} = \int_0^\infty \frac{d^2 \bar{n}(z, \text{SNR} \geq 10)}{dz} \frac{dz}{dt} \frac{dV_c}{dz} \frac{dz}{(1+z)}, \quad (21)$$

where  $dz/dt$  is given by

$$dz/dt = -(1+z)H_0\sqrt{E(z)}, \quad (22)$$

where  $H_0$  is the present value of the Hubble constant, 70000 m/s/Mpc and  $E(z)$  is given by

$$E(z) = (1+z)^2(1 + \Omega_M z) - z(2+z)\Omega_\Lambda, \quad (23)$$

The quantity  $dV_c/dz$  is the comoving volume in a redshift interval between  $z$ , and  $z + dz$  as follows:

$$\frac{dV_c}{dz} = 4\pi \left(\frac{c}{H_0}\right)^3 \frac{1}{\sqrt{E(z)}} \left[ \int_0^z \frac{1}{\sqrt{E(z')}} dz' \right]^2, \quad (24)$$

So the total number of events detected per observed time is:

$$N_{\text{total}} = \int_0^{T_{\text{obs}}} \frac{d\bar{N}}{dt_{\text{obs}}} dt_{\text{obs}}. \quad (25)$$

To determine the number of resolvable events of the inspiral and merger-ringdown sources from the BBHs in the simulations, we consider a signal with  $\text{SNR} \geq 10$  whose observed merger frequency falls in the target detector’s frequency range (see Table 1) as detectable. We select all the signals that satisfy these conditions to obtain the resolvable signals for each detector. To predict the event rate of these sources for each detector, we assume an observational time duration of 3 years as this is the proposed lifetime of many of the detectors. Furthermore, since our simulations do not have the necessary resolution to determine the spin of each individual BH, we quantify the effect of spin on the estimates by using the minimum and maximum spins for the merging BH pairs (i.e.  $\chi_1=0$ ,  $\chi_2=0$ , and  $\chi_1=1, \chi_2=1$ ) as the bracketing error bars.

Table 2 lists the estimates of resolvable signals and event rates of inspiral, merger-ringdown, and full inspiral-merger-ringdown sources from all six zoom-in simulations with different BH seeds for both space- and ground-based GW detectors. Here are a number of remarks on the results:

- First of all, the BBH events in all the six simulations fall outside of the frequency range of the Advanced LIGO – Advanced Virgo network, so it will not be able to resolve any of the high-redshift BH mergers from our simulations.
- The third-generation ground-based “3G” network of ET-D and CE has the outstanding capacity to detect signals from low-mass BH mergers of  $\sim 10^1 - 10^3 M_\odot$  up to redshift  $z \sim 21$ , with a detection rate of  $\sim 10^3/\text{yr}$  for inspiral sources and  $\sim 2 \times 10^3/\text{yr}$  for mergers events per year, which increases the detection rate by a factor of  $\sim 2 - 10$  compared to individual detector of CE (corresponding detection rate  $\sim 470$  and  $1240$  per year, respectively) and ET-D ( $\sim 72, 190$  per year, respectively).
- On the other hand, space-based detectors can detect BBHs of a wider mass range. LISA will be able to detect both BBH inspirals and mergers of  $\sim 10^3 - 10^7 M_\odot$  in the redshift range  $z \sim 23 - 6$ . The detection rate of BH mergers at high redshift  $z \geq 6$  depends sensitively on the mass, from  $\sim 10/\text{yr}$  for mergers of  $10^3 - 10^4 M_\odot$ , to  $\sim 40/\text{yr}$  for  $10^4 - 10^5 M_\odot$  mergers, down to  $\sim 4/\text{yr}$  for BH mergers of  $\geq 10^5 M_\odot$ .
- Between “G3” and LISA, DECIGO and BBO will be able to resolve BH mergers of  $10^1 - 10^5 M_\odot$ . In particular, they can detect  $\sim 1700$  inspiral sources and  $\sim 800 - 1000$  mergers of  $10^1 - 10^3 M_\odot$  per year. For a higher mass range of  $10^2 - 10^4 M_\odot$ , they can detect  $\sim 1900$  inspiral and mergers per year, respectively.
- In general, all the detectors appear to have higher detection rates of BBH mergers originated from  $10^2 M_\odot$  seeds. Detection of BBH mergers of  $\sim 10^2 - 10^4 M_\odot$  at the cosmic dawn ( $z \sim 23 - 6$ ) holds the key to understanding the BH seed models, in particular the light seeds ( $\sim 10^1 - 10^2 M_\odot$ ) that form from Pop III stars.
- The synergy between ground- and space-based detectors will be able to detect 10% of the BBHs in the mass range of  $\sim 10^1 - 10^7 M_\odot$  in the redshift range of  $z \sim 23 - 6$  from all the simulations. However, we caution that because these zoom-in simulations are focused on highly overdense regions, the estimated rates may be biased, and it is non-trivial to extrapolate the event rates in Table 2 to a cosmic volume of the entire observable Universe.

### 3.4 Redshift Distributions of Detectable Events

The redshift distribution of BBH merger events is an important indicator of the environments in which they grow, the star formation rate (SFR), and the distribution of time delays (Mapelli et al. 2017; Mapelli & Giacobbo 2018; Fishbach et al. 2018). It offers a powerful tool to distinguish between different channels by which BBHs form. For example, an isolated binary channel facilitates redshift evolutions related to the SFR and time delays between formation and merger (Abbott et al. 2016b) while a dynamical formation channel ties the evolution of BBH merger to that of globular clusters (Rodríguez & Loeb 2018; Antonini, Fabio and Gieles, Mark 2020; Kritos & Cholis 2020). It is important to add here that the redshift distribution is influenced by the total redshifted mass of the BBH system. At high redshifted mass, higher harmonics of the multimodal radiation of the GW sources will contribute more to the SNRs. This effect of this contribution will be more significant for third generation detectors that can detect mergers at higher redshifts than current generation of detectors such as aLIGO (Dominik et al. 2015). The redshift distribution can be indirectly obtained by measuring the luminosity distance to the GW sources.

Figure 5 shows the redshift distributions of the inspiral and merger-ringdown events occurring in each of the zoom-in simulations, resolvable by various GW detectors. Note that the

**Table 2.** Estimates of resolvable signals ( $\text{SNR} \geq 10$ ) and event rates of inspiral, merger-ringdown (Mrd), and full inspiral-merger-ringdown (full-IMR) sources from the six simulations for various gravitational wave detectors, including the “3G” network of CE and ET-D, LISA, and DECIGO/BBO which have similar frequency range and detection capacities.

Simulation	Number of Resolvable Inspirational Signals			Number of Resolvable Mrd Signals			Number of full-IMR Signals			Number of merger events
BH seed mass	3G	LISA	DECIGO/BBO	3G	LISA	DECIGO/BBO	3G	LISA	DECIGO/BBO	
$10^1 M_\odot$	11515 $\pm$ 1788	261 $\pm$ 9	18689 $\pm$ 34	22915 $\pm$ 327	93 $\pm$ 33	9837 $\pm$ 1135	22917 $\pm$ 191	102 $\pm$ 24	18731 $\pm$ 1	29987
$10^2 M_\odot$	0	475 $\pm$ 56	4882 $\pm$ 1	727 $\pm$ 169	457 $\pm$ 23	4882 $\pm$ 1	727 $\pm$ 288	320 $\pm$ 28	4882 $\pm$ 1	5283
$10^3 M_\odot$	0	64 $\pm$ 1	38 $\pm$ 2	0	73 $\pm$ 3	36 $\pm$ 2	0	74 $\pm$ 3	38 $\pm$ 2	78
$10^4 M_\odot$	0	36 $\pm$ 6	12 $\pm$ 1	0	44 $\pm$ 1	12 $\pm$ 1	0	44 $\pm$ 1	12 $\pm$ 1	57
$10^5 M_\odot$	0	23 $\pm$ 2	1	0	52 $\pm$ 1	1	0	53	1	60
$10^6 M_\odot$	0	1	0	0	41 $\pm$ 2	0	0	42 $\pm$ 1	0	57
BH seed mass	Detection Rates Of Inspirational Signals ( $\text{yr}^{-1}$ )			Detection Rates Of Mrd Signals ( $\text{yr}^{-1}$ )			Detection Rates Of full-IMR Signals ( $\text{yr}^{-1}$ )			Redshift Range
$10^1 M_\odot$	1001 $\pm$ 170	21.2 $\pm$ 0.8	1695 $\pm$ 3	2059 $\pm$ 30	7.3 $\pm$ 2.7	873 $\pm$ 101	2059 $\pm$ 30	8.0 $\pm$ 1.9	1698 $\pm$ 1	21.0 – 5.7
$10^2 M_\odot$	0	41 $\pm$ 5	454 $\pm$ 1	62 $\pm$ 15	44 $\pm$ 3	454 $\pm$ 1	62 $\pm$ 15	44 $\pm$ 2	454 $\pm$ 1	23 – 6
$10^3 M_\odot$	0	5.4 $\pm$ 0.1	3.1 $\pm$ 0.1	0	6.1 $\pm$ 0.2	3.1 $\pm$ 0.1	0	6.1 $\pm$ 0.2	3.1 $\pm$ 0.1	13.2 – 6.2
$10^4 M_\odot$	0	3.0 $\pm$ 0.5	1.0 $\pm$ 0.1	0	3.3 $\pm$ 0.3	1.0 $\pm$ 0.1	0	3.7 $\pm$ 0.1	1.0 $\pm$ 0.1	11.5 – 6.0
$10^5 M_\odot$	0	1.9 $\pm$ 0.2	0.0	0	4.4 $\pm$ 0.1	0.0	0	4.5 $\pm$ 0.2	0	11.8 – 6.1
$10^6 M_\odot$	0	0	0	0	3.7 $\pm$ 0.1	0	0	3.7 $\pm$ 0.1	0	11.2 – 6.2

Notes:

1. aLIGO will not be able to detect any of the BH mergers in the simulations, and ET-D and CE can only detect events in the  $M_{\text{seed}} = 10 M_\odot$  simulation.
2. For ET-D, the number of resolvable inspiral, merger-ringdown, and full-IMR events from the  $M_{\text{seed}} = 10 M_\odot$  simulation are  $979 \pm 2$ ,  $2499 \pm 8$ , and  $2495 \pm 45$ , respectively. The corresponding detection rates are  $72 \pm 1$ ,  $188 \pm 1$ , and  $191 \pm 4$  events per year.
3. For CE, the number of resolvable inspiral, merger-ringdown and full-IMR events from the  $M_{\text{seed}} = 10 M_\odot$  simulation are  $6678 \pm 443$ ,  $13963 \pm 3$ , and  $13953 \pm 12$ , respectively. The corresponding detection rates are  $472 \pm 39$ ,  $1240 \pm 1$ , and  $1234 \pm 7$ , respectively.
4. The errors are estimated using minimum and maximum spins for the merging BH pairs (i.e.  $\chi_1=0$ ,  $\chi_2=0$ , and  $\chi_1=1, \chi_2=1$ ), since our simulations do not have the necessary resolution to determine the spin of each individual BH.
5. The BH seed mass is the mass of the BH seed in each simulation, not the mass of the BH mergers in the inspiral or merger phases, which are usually more massive than the seeds.

merger redshift is different from the formation redshift when the BBHs form, so it is better applied to the Merger-Ringdown phase. Nevertheless, this Figure illustrates the redshift range and the estimated number of events one may expect. In particular, it demonstrates that the 3G CE-ET network has great potential for detecting the BH mergers that originate from low-mass seeds ( $10^1 - 10^2 M_\odot$ ) from the Pop III stars at high redshifts, while LISA is poised to detect more massive BBHs in the same period. Being in the deci-hertz window, DECIGO and BBO have similar capabilities, and they will bridge the gap between 3G CE-ET network and LISA by detecting BBHs in the intermediate mass range. A combination of all these detectors will provide unprecedented insights on the earliest BHs, which may ultimately reveal the origin of the astrophysical BHs that we observe from the cosmic dawn to the present day.

#### 4 DISCUSSION

Our calculations provide a new method to study BHs in the early Universe and the assembly of the first SMBHs and quasars. However, we stress that our model is *phenomenological* and that there are a number of caveats that may affect our results.

**First of all, our zoom-in simulations focus on highly over-dense regions and massive halos where galaxy interactions and BH mergers may be more frequent than average regions with mean density, so our results may be biased, and the estimated event rates from these simulations should not be interpreted as the detection rate for the entire observable Universe RS:** (see also Valiante et al. 2020 for a discussion on this issue).

Moreover, our cosmological simulations have limited resolution, and cannot resolve low-mass BHs and tightly bound BBHs, which would affect the estimate of BH mass growth, and the merger rates and merging timescales of BBHs. As discussed in detail in Zhu et al. (2020), we used a “ghost particle” technique to treat small BHs ( $10 - 10^2 M_\odot$ ) that form from PopIII stars by associating the

new BH with its more massive parent star particle (the “ghost”), such that the BHs have the same dynamics as their “ghosts” while keeping their own mass growth through accretion and mergers. This numerical technique may affect the dynamics of BBHs and overestimate the merger rate as the “ghost particles” have larger collisional cross sections than the BHs.

Furthermore, for BBH pairs within the spatial resolution, we adopt a simple scheme to add a time delay to the inspiral phase until they merge. However, previous studies showed that the length of time between the point when BHs pass within the resolution limit and enter the inspiral phase depends on many factors associated with the stellar and gas distributions in the vicinity of the BHs, and that there can be a substantial delay until the binary enters the inspiral phase (Kelley et al. 2017, 2018; Siwek et al. 2020). Therefore, our treatment of the inspiral phase may underestimate the timescale of the merger.

Last but not least, in our simulations, BH kicks from gravitational recoil during BH–BH mergers is not included. Sijacki et al. (2009) showed that gravitational recoil would affect BH accretion and may result in lower BH mass by a factor of a few, but SMBHs in massive galaxies can rarely escape due to steep potential well. As pointed out in Zhu et al. (2020), because the host galaxy in our simulations is very massive and gas rich, it has an escape velocity of  $> 10^3 \text{ km/s}$  at  $z \sim 6.5$ , therefore, the impact of gravitational recoil on the BH mergers in our simulations may be insignificant.

**Overall, with these caveats in mind, a strong result from our calculations is that a synergy between the ground- and space-based GW detectors will be able to detect BBHs in the wide mass range of  $\sim 10^1 - 10^7 M_\odot$  in the redshift range of  $z \sim 23 - 6$ , with a rate that account for  $\sim 10\%$  of the BBH coalescence events that take place during the assembly of the first SMBHs.**

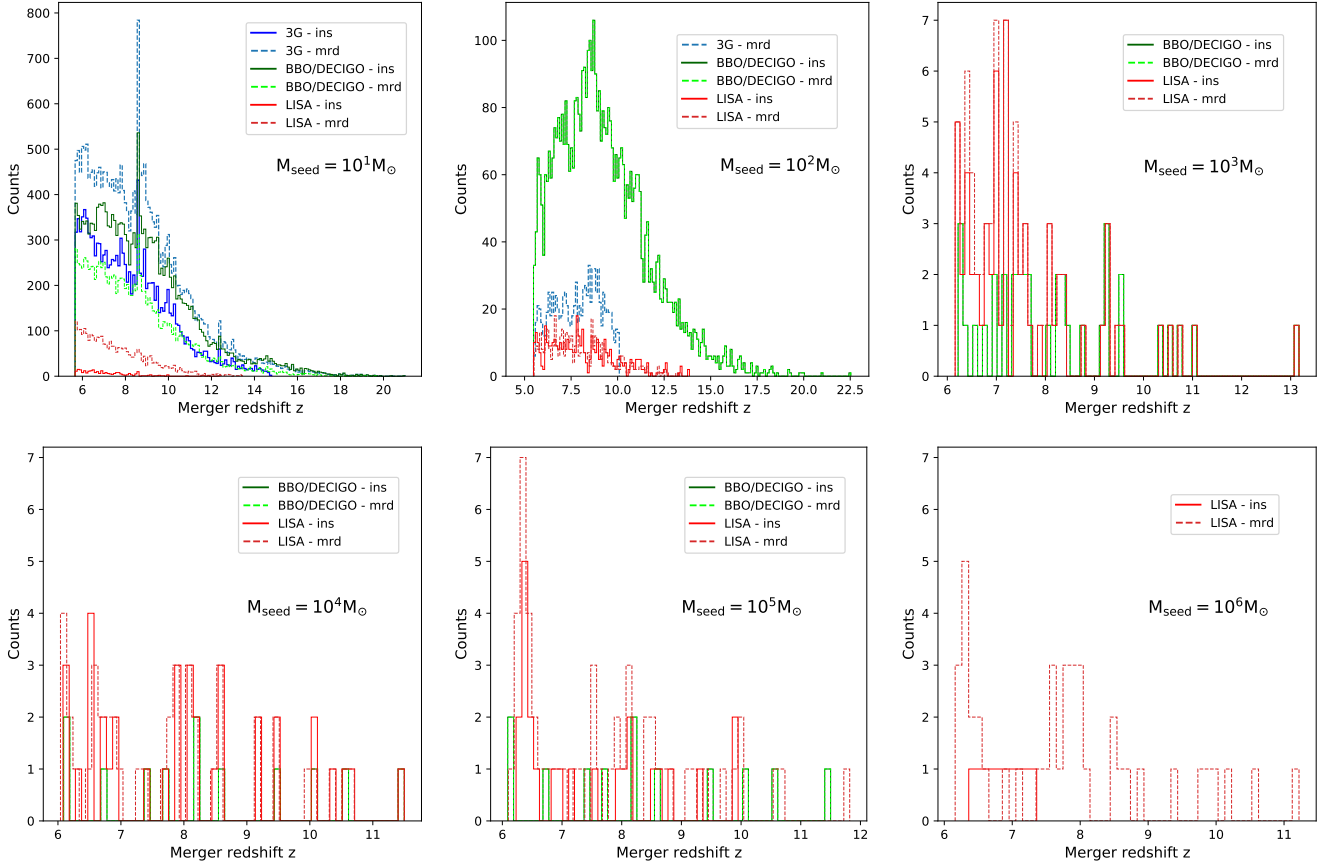


**Figure 5.** The redshift distributions of all the inspiral and merger-ringdown sources from the six simulations resolvable by the “3G” CE-ET network, LISA, and BBO /DECIGO detectors, respectively. Note BBO /DECIGO have similar frequency ranges and detection sensitivity curves. For each instrument, the solid line represents the inspiral signals, while the dashed line represents the merger-ringdown events. YL: The signals here are computed from spin 0 black holes using a redshift bin size of 0.1.

## 5 CONCLUSIONS

To summarize, we have calculated GW signals from BH mergers of a wide mass range  $\sim 10^1 - 10^7 M_{\odot}$  at high redshifts  $z \sim 23 - 6$  during the assembly of the first quasars, by post-processing the merger trees extracted from six cosmological zoom-in simulations with a phenomenological GW model. Here is a summary of our main findings:

- (i) Numerous BH mergers may occur during the assembly of the first SMBHs and quasars regardless of the seed mass, and these merger events may be detectable by ground- and space-based GW detectors. The detection rate depends sensitively on the mass and occurrence time of the BH coalescence events.
- (ii) The third-generation ground-based 3-detector-network “G3” of CE and ET-D has the greatest potential to detect BH mergers from light BH seeds  $\sim 10^1 - 10^2 M_{\odot}$  that likely form from Pop III stars at high redshifts  $z \sim 23 - 6$ , reaching a detection rate of  $\sim 1 - 2 \times 10^3/\text{yr}$ , which is a significant improvement over individual CE or ET-D detectors.
- (iii) Space-based detectors can detect BBHs of a wider mass range. LISA will be able to detect both BBH inspirals and mergers of  $\sim 10^3 - 10^7 M_{\odot}$  with an estimated event rate of  $\sim 10\text{s}/\text{yr}$  in the redshift range  $z \sim 23 - 6$ .

- (iv) The space-based BBO and DECIGO will bridge the gap between “G3” and LISA, and they can detect BBH inspirals and mergers in the intermediate-mass range of  $10^2 - 10^4 M_{\odot}$ , with a rate of  $\sim 1 - 2 \times 10^3/\text{yr}$  at redshifts  $z \sim 21 - 6$ .
- (v) A combination of ground- and space-based detectors will be able to detect 10% of the BBHs in the mass range of  $\sim 10^1 - 10^7 M_{\odot}$  in the redshift range of  $z \sim 23 - 6$  in the formation and evolution of the first galaxies and quasars.

These results demonstrate that GW detectors will be powerful tools to study BHs in the early Universe, and that a synergy between ground- and space-based detectors will be able to detect BH mergers over a wide range of mass at high redshifts  $z \sim 23 - 6$ , which will be promising to probe different BH seed models and unravel the origin of the SMBHs that power the most distant quasars we observed at the cosmic dawn.

## ACKNOWLEDGMENTS

We thank Dr. Mark Hannam for providing the code of the PhenomD model for gravitational waves calculations. YL acknowledges support from NSF grants AST-1412719 and MRI-1626251. QZ is supported by the McWilliams Fellowship from The McWilliams Center



for Cosmology at Carnegie Mellon University. YL and RS acknowledge support from the Amaldi Research Center funded by the MIUR program “Dipartimento di Eccellenza” (CUP:B81I18001170001), and from the INFN TEONGRAV specific initiative. HY acknowledges support from MEXT/JSPS KAKENHI Grant Number 17H04827, 20H04724, and NAOJ ALMA Scientific Research Grant Numbers 2019-11A. The numerical computations and data analysis in this paper have been carried out on the CyberLAMP cluster supported by MRI-1626251, operated and maintained by the Penn State Institute for Computational and Data Sciences. The Institute for Gravitation and the Cosmos is supported by the Eberly College of Science and the Office of the Senior Vice President for Research at the Pennsylvania State University.

## DATA AVAILABILITY

The simulation data produced in this research will be shared on reasonable request to the corresponding author.

## REFERENCES

- Abbott B. P., et al., 2016a, *Phys. Rev. Lett.*, 116, 061102
- Abbott B. P., et al., 2016b, *The Astrophysical Journal*, 818, L22
- Abbott B. P., et al., 2017, *Class. Quant. Grav.*, 34, 044001
- Abbott R., et al., 2020a, arXiv e-prints, [p. arXiv:2010.14527](#)
- Abbott R., et al., 2020b, *Phys. Rev. Lett.*, 125, 101102
- Amaro-Seoane P., et al., 2017, preprint, ([arXiv:1702.00786](#))
- Antonini, Fabio and Gies, Mark 2020
- Bañados E., et al., 2018, *Nature*, 553, 473
- Barausse E., Matarrese S., Riotto A., 2005, *Phys. Rev. D*, 71, 063537
- Barausse E., Morozova V., Rezzolla L., 2012, *ApJ*, 758, 63
- Blanchet L., 2014, *Living Reviews in Relativity*, 17, 2
- Buonanno A., Damour T., 1999, *Phys. Rev. D*, 59, 084006
- Buonanno A., Sathyaprakash B. S., 2014, arXiv 1410.7832,
- Colpi M., et al., 2019, arXiv e-prints, [p. arXiv:1903.06867](#)
- Crowder J., Cornish N. J., 2005, *Phys. Rev. D*, 72, 083005
- DeGraf C., Sijacki D., 2020, *MNRAS*, 491, 4973
- Dominik M., et al., 2015, *The Astrophysical Journal*, 806, 263
- Finn L. S., Thorne K. S., 2000, *Phys. Rev. D*, 62, 124021
- Fishbach M., Holz D. E., Farr W. M., 2018, *The Astrophysical Journal*, 863, L41
- Flanagan É. É., Hughes S. A., 1998, *Phys. Rev. D*, 57, 4566
- Glover S. C. O., 2015a, *MNRAS*, 451, 2082
- Glover S. C. O., 2015b, *MNRAS*, 453, 2901
- Greene J. E., Strader J., Ho L. C., 2020, arXiv e-prints, [p. arXiv:1911.09678](#)
- Haehnelt M. G., 1994, *MNRAS*, 269, 199
- Hopkins P. F., 2015, *MNRAS*, 450, 53
- Husa S., Khan S., Hannam M., Pürrer M., Ohme F., Forteza X. J., Bohé A., 2016, *Phys. Rev. D*, 93, 044006
- Inayoshi K., Visbal E., Haiman Z., 2020, *ARA&A*, 58, 27
- Israel W., 1968, *Communications in Mathematical Physics*, 8, 245
- Kalogera V., et al., 2019, *BAAS*, 51, 242
- Katz M. L., Larson S. L., 2018, *Monthly Notices of the Royal Astronomical Society*, 483, 3108
- Katz H., Sijacki D., Haehnelt M. G., 2015, *MNRAS*, 451, 2352
- Katz M. L., Kelley L. Z., Dosopoulou F., Berry S., Blecha L., Larson S. L., 2020, *MNRAS*, 491, 2301
- Kawamura S., et al., 2020, arXiv e-prints, [p. arXiv:2006.13545](#)
- Kelley L. Z., Blecha L., Hernquist L., Sesana A., Taylor S. R., 2017, *Monthly Notices of the Royal Astronomical Society*, 471, 4508
- Kelley L. Z., Blecha L., Hernquist L., Sesana A., Taylor S. R., 2018, *Monthly Notices of the Royal Astronomical Society*, 477, 964
- Koushiappas S. M., Zentner A. R., 2006, *ApJ*, 639, 7
- Kritos K., Cholis I., 2020, *Phys. Rev. D*, 102, 083016
- Kumar P., et al., 2016, *Phys. Rev. D*, 93, 104050
- Li Y., et al., 2007, *The Astrophysical Journal*, 665, 187
- Li Y., et al., 2008, *ApJ*, 678, 41
- Luo J., et al., 2016, *Classical and Quantum Gravity*, 33, 035010
- Luo Y., Shlosman I., Nagamine K., Fang T., 2020, *MNRAS*, 492, 4917
- Lupi A., Haardt F., Dotti M., Fiacconi D., Mayer L., Madau P., 2016, *MNRAS*, 456, 2993
- Madau P., Haardt F., Dotti M., 2014, *ApJ*, 784, L38
- Maggiore M., et al., 2020, *J. Cosmology Astropart. Phys.*, 2020, 050
- Mapelli M., Giacobbo N., 2018, *MNRAS*, 479, 4391
- Mapelli M., Giacobbo N., Ripamonti E., Spera M., 2017, *MNRAS*, 472, 2422
- Moore C. J., Cole R. H., Berry C. P. L., 2015, *Classical and Quantum Gravity*, 32, 015014
- Mortlock D. J., et al., 2011, *Nature*, 474, 616
- Pacucci F., Volonteri M., Ferrara A., 2015, *MNRAS*, 452, 1922
- Pezzulli E., Valiante R., Schneider R., 2016, *MNRAS*, 458, 3047
- Pezzulli E., Valiante R., Orofino M. C., Schneider R., Gallerani S., Sbarrato T., 2017, *MNRAS*, 466, 2131
- Planck Collaboration et al., 2016, *A&A*, 594, A13
- Punturo M., et al., 2010, *Class. Quant. Grav.*, 27, 194002
- Regan J. A., Visbal E., Wise J. H., Haiman Z., Johansson P. H., Bryan G. L., 2017, *Nature Astronomy*, 1, 0075
- Reitze D., et al., 2019, in *Bulletin of the American Astronomical Society*, p. 35 ([arXiv:1907.04833](#))
- Ricarte A., Natarajan P., 2018, *MNRAS*, 481, 3278
- Rodriguez C. L., Loeb A., 2018, *ApJ*, 866, L5
- Ruan W.-H., Guo Z.-K., Cai R.-G., Zhang Y.-Z., 2018, arXiv e-prints, [p. arXiv:1807.09495](#)
- Salcido J., Bower R. G., Theuns T., McAlpine S., Schaller M., Crain R. A., Schaye J., Regan J., 2016, *MNRAS*, 463, 870
- Sathyaprakash B., Dhurandhar S., 1991, *Phys. Rev. D*, 44, 3819
- Sathyaprakash B. S., Schutz B. F., 2009, *Living Reviews in Relativity*, 12, 2
- Sathyaprakash B., et al., 2012, *Classical and Quantum Gravity*, 29, 124013
- Scharre P. D., Will C. M., 2002, *Phys. Rev. D*, 65, 042002
- Schmitz K., 2020, arXiv e-prints, [p. arXiv:2002.04615](#)
- Schutz B. F., Sathyaprakash B. S., 2020, arXiv e-prints, [p. arXiv:2009.10212](#)
- Sesana A., 2013, *Classical and Quantum Gravity*, 30, 244009
- Sesana A., Haardt F., Madau P., Volonteri M., 2004, *ApJ*, 611, 623
- Shapiro S. L., Teukolsky S. A., 1983, *Black holes, white dwarfs, and neutron stars: The physics of compact objects*
- Sijacki D., Springel V., Haehnelt M. G., 2009, *Monthly Notices of the Royal Astronomical Society*, 400, 100
- Siwek M. S., Kelley L. Z., Hernquist L., 2020, *Monthly Notices of the Royal Astronomical Society*, 498, 537
- Springel V., Hernquist L., 2003, *MNRAS*, 339, 289
- Springel V., Di Matteo T., Hernquist L., 2005, *MNRAS*, 361, 776
- Tanaka T., Menou K., Haiman Z., 2012, *MNRAS*, 420, 705
- The LIGO Scientific Collaboration et al., 2020, arXiv e-prints, [p. arXiv:2010.14533](#)
- Valiante R., Schneider R., Volonteri M., Omukai K., 2016, *MNRAS*, 457, 3356
- Valiante R., Agarwal B., Habouzit M., Pezzulli E., 2017, *Publ. Astron. Soc. Australia*, 34, e031
- Valiante R., Schneider R., Graziani L., Zappacosta L., 2018a, *MNRAS*, 474, 3825
- Valiante R., Schneider R., Zappacosta L., Graziani L., Pezzulli E., Volonteri M., 2018b, *MNRAS*, 476, 407
- Valiante R., et al., 2020, *MNRAS*, 500, 4095
- Vishveshwara C. V., 1970, *Nature*, 227, 936
- Vitale S., Whittle C., 2018, *Phys. Rev. D*, 98, 024029
- Vito F., et al., 2019, *A&A*, 630, A118
- Vogelsberger M., Genel S., Sijacki D., Torrey P., Springel V., Hernquist L., 2013, *MNRAS*, 436, 3031
- Volonteri M., et al., 2020, *MNRAS*, 498, 2219
- Wiersma R. P. C., Schaye J., Smith B. D., 2009, *MNRAS*, 393, 99
- Wise J. H., Regan J. A., O’Shea B. W., Norman M. L., Downes T. P., Xu H., 2019, *Nature*, 566, 85

- Woods T. E., Heger A., Whalen D. J., Haemmerlé L., Klessen R. S., 2017, [ApJ](#), 842, L6
- Woods T. E., et al., 2019, [Publ. Astron. Soc. Australia](#), 36, e027
- Wu X.-B., et al., 2015, [Nature](#), 518, 512
- Wyithe J. S. B., Loeb A., 2003, [ApJ](#), 590, 691
- Yagi K., Seto N., 2011, [Phys. Rev. D](#), 83, 044011
- Yajima H., Khochfar S., 2016, [MNRAS](#), 457, 2423
- Zhu Q., Li Y., 2016, [ApJ](#), 831, 52
- Zhu Q., Li Y., Maji M., Yajima H., Schneider R., Hernquist L., 2020, arXiv e-prints, [p. arXiv:2012.01458](#)

This paper has been typeset from a  $\text{\LaTeX}$  file prepared by the author.